



HAL
open science

Elastic and anelastic structure of the lowermost mantle beneath the Western Pacific from waveform inversion

Kensuke Konishi, Nobuaki Fuji, Frédéric Deschamps

► To cite this version:

Kensuke Konishi, Nobuaki Fuji, Frédéric Deschamps. Elastic and anelastic structure of the lowermost mantle beneath the Western Pacific from waveform inversion. *Geophysical Journal International*, 2017, 208, pp.1290-1304. <10.1093/gji/ggw450>. <insu-03748871>

HAL Id: insu-03748871

<https://insu.hal.science/insu-03748871v1>

Submitted on 10 Aug 2022

HAL is a multi-disciplinary open access archive for the deposit and dissemination of scientific research documents, whether they are published or not. The documents may come from teaching and research institutions in France or abroad, or from public or private research centers.

L'archive ouverte pluridisciplinaire HAL, est destinée au dépôt et à la diffusion de documents scientifiques de niveau recherche, publiés ou non, émanant des établissements d'enseignement et de recherche français ou étrangers, des laboratoires publics ou privés.



Distributed under a Creative Commons CC BY 4.0 - Attribution - International License

Elastic and anelastic structure of the lowermost mantle beneath the Western Pacific from waveform inversion

Kensuke Konishi,¹ Nobuaki Fuji² and Frédéric Deschamps¹

¹*Institute of Earth Sciences, Academia Sinica, 128 Academia Road Sec. 2, Nangang, Taipei 11529, Taiwan. E-mail: kensuke@earth.sinica.edu.tw*

²*Institut de Physique du Globe de Paris, 1 rue Jussieu, F-75238 Paris Cedex 05, France*

Accepted 2016 November 30. Received 2016 November 21; in original form 2016 June 14

SUMMARY

We investigate the elastic and anelastic structure of the lowermost mantle at the western edge of the Pacific large low shear velocity province (LLSVP) by inverting a collection of *S* and *ScS* waveforms. The transverse component data were obtained from F-net for 31 deep earthquakes beneath Tonga and Fiji, filtered between 12.5 and 200 s. We observe a regional variation of *S* and *ScS* arrival times and amplitude ratios, according to which we divide our region of interest into three subregions. For each of these subregions, we then perform 1-D (depth-dependent) waveform inversions simultaneously for radial profiles of shear wave velocity (V_S) and seismic quality factor (Q). Models for all three subregions show low V_S and low Q structures from 2000 km depth down to the core–mantle boundary. We further find that V_S and Q in the central subregion, sampling the Caroline plume, are substantially lower than in the surrounding regions, whatever the depth. In the central subregion, V_S -anomalies with respect to PREM (dV_S) and Q are about -2.5 per cent and 216 at a depth of 2850 km, and -0.6 per cent and 263 at a depth of 2000 km. By contrast, in the two other regions, dV_S and Q are -2.2 per cent and 261 at a depth of 2850 km, and -0.3 per cent and 291 at a depth of 2000 km. At depths greater than ~ 2500 km, these differences may indicate lateral variations in temperature of ~ 100 K within the Pacific LLSVP. At shallower depths, they may be due to the temperature difference between the Caroline plume and its surroundings, and possibly to a small fraction of iron-rich material entrained by the plume.

Key words: Inverse theory; Elasticity and anelasticity; Body waves; Seismic attenuation; Seismic tomography; Pacific Ocean.

1 INTRODUCTION

Global-scale studies of the lowermost mantle structure have revealed large-scale heterogeneities of shear wave velocity (V_S) with amplitude up to a few per cent (e.g. Panning & Romanowicz 2006; Houser *et al.* 2008; Kustowski *et al.* 2008; Simmons *et al.* 2009; Ritsema *et al.* 2011; Takeuchi 2012). While discrepancies remain on the details of the observed structures, all recent models agree on the existence of two ‘large low shear velocity provinces’ (called LLSVPs) beneath the Pacific and Africa. Interestingly, LLSVPs are also observed in global V_S models obtained from normal modes data (Ishii & Tromp 1999; Trampert *et al.* 2004), suggesting that these structures are not artefacts due to an uneven coverage of seismic sources and stations. The origin, purely thermal or thermochemical, of these velocity anomalies is still controversial (for recent discussions, see Davies *et al.* 2015; Deschamps *et al.* 2015; Garnero *et al.* 2016). Based on the combination between V_S and density anomalies, these later studies favour a thermochemical origin.

Because they are all based on low frequency global seismological data, global studies cannot constrain the details of LLSVPs and local structures. Recovering such details requires local or regional data

sets, sampling a specific region. Using *SKS* waveforms and *ScS* and *SKS* traveltimes, Ni *et al.* (2002) showed that the African LLSVP has sharp boundaries and that its southern tip is tilted to the east. Waveform studies for the Pacific LLSVP have also reported sharp edges (To *et al.* 2005; Takeuchi *et al.* 2008), and further suggested that this LLSVP may split into two distinct provinces (He & Wen 2009). More investigations of local structures with high-frequency body waves are still needed for a better description of LLSVPs. Furthermore, additional constraints, different from seismic wave speeds, may be useful to resolve the thermal and chemical contributions to seismic anomalies. Since it strongly depends on temperature, seismic attenuation, which is usually expressed in terms of seismic quality factor (Q), is potentially an interesting additional seismic parameter to investigate.

Here, we apply a simultaneous waveform inversion method for elasticity and anelasticity (Fuji *et al.* 2010) to a data set collected from F-net to recover 1-D radial profiles of V_S and Q at three locations in the western tip of the Pacific LLSVP. For this region, global V_S models SEMUCB-WM1 (French & Romanowicz 2015) and S40RTS (Ritsema *et al.* 2011) map substantial lateral variations within the Pacific LLSVP, in particular around the Caroline plume,

Table 1. Earthquakes used in this study.

Event #	Date (Y/M/D)	Latitude	Longitude	Depth	M_W	Global CMT id
1	2002 January 2	−17.63	178.84	680.8	6.1	010202E
2	2004 January 11	−16.27	−176.05	381.4	5.9	011104B
3	2000 May 4	−17.72	−178.31	539.8	6.4	050400K
4	2003 May 19	−18.02	−178.42	578.5	5.9	051903B
5	2002 June 16	−17.65	−178.5	588.1	5.9	061602C
6	2002 August 9	−16.25	−175.85	381.3	6.1	080902B
7	2003 October 15	−17.84	−178.59	594.9	5.9	101503A
8	2002 October 17	−19.8	−178.23	621.9	6.1	101702C
9	2001 November 5	−17.12	−178.96	579.7	6.2	110501D
10	2002 December 28	−18.0	−178.4	635.5	5.8	122802A
11	2006 February 24	−17.94	−179.42	640.9	6.1	200602241415A
12	2006 June 9	−17.36	−178.62	585.9	6.1	200606090558A
13	2006 July 23	−17.97	−178.42	597.9	5.8	200607232050A
14	2007 March 23	−18.87	−178.24	644.6	5.8	200703232230A
15	2007 April 9	−20.0	−177.97	613.7	5.9	200704090224A
16	2007 May 6	−19.44	−179.04	690.8	6.5	200705062111A
17	2007 May 6	−19.31	−179.05	691.6	6.0	200705062201A
18	2007 May 13	−19.58	−179.03	694.9	5.8	200705131126A
19	2008 April 18	−17.26	−178.98	577.8	6.3	200804182039A
20	2008 June 15	−17.77	−179.66	623.6	5.9	200806150113A
21	2008 December 17	−17.77	−178.3	547.8	5.8	200812171055A
22	2009 January 26	−17.83	−178.55	616.5	5.8	200901261154A
23	2009 January 27	−17.81	−178.51	612.7	5.9	200901270629A
24	2009 March 5	−17.46	−178.9	553.3	5.9	200903051933A
25	2009 November 22	−17.72	−178.36	546.4	6.3	200911220748A
26	2010 June 22	−19.16	−177.49	587.4	5.8	201006222216A
27	2011 April 3	−17.65	−178.45	562.3	6.4	201104031407A
28	2011 August 19	−16.52	−176.73	415.0	6.2	201108190354A
29	2011 October 27	−17.98	−179.4	608.7	6.0	201110270015A
30	2012 February 10	−17.98	−178.42	598.0	5.9	201202100147A
31	2013 November 23	−17.09	−176.38	386.6	6.5	201311230748A

located at 5°N, 164°E. At shallower depths, SEMUCB-WM1 further observes a vertical conduit of low V_S rooted in the LLSVP, and corresponding to the Caroline plume. Hints for lateral variations in V_S in the western tip of the Pacific LLSVP and low V_S associated with the Caroline plume have also been mapped by Takeuchi (2012). We observe clear differences, both in V_S and Q between a profile sampling the Caroline plume and the two other profiles sampling its surroundings. Interestingly, such a localized V_S structure is observed in a 3-D model obtained by waveform inversion (Konishi *et al.* 2014).

2 DATA SET AND PRE-PROCESSING

In order to image the lowermost mantle beneath the western Pacific in a layer ranging from a depth of 2000 km down to the core–mantle boundary (CMB), at 2891 km, we collected broadband waveform data from the Japanese network F-net (77 stations) for 31 deep earthquakes (Table 1) having occurred in the vicinity of Fiji islands. The data set used in waveform inversion consists of 1341 velocity seismograms. Fig. 1 shows the geometry of sources and seismic stations, as well as projections of ray paths of direct waves. Note that, in this study, we only invert transverse component in order to infer SH -wave velocity structure. We first calculated synthetic waveforms for the ‘PREM’ model’ (Konishi *et al.* 2009), which is a 1-D model modified from Preliminary Reference Earth Model (PREM; Dziewonski & Anderson 1981), and is well suited for this region. PREM’ was obtained by forward-modelling of several ‘PREM-like’ models with different lowermost mantle V_S structures, so that the synthetics fit better the observed data for the western

Pacific (Konishi *et al.* 2009). The only difference between PREM’ and PREM is that the mean V_S in D’ region in PREM’ is lower than that in PREM by ~ 1.5 per cent. We analysed discrepancies between observed and synthetic data by systematically looking at two seismic observables, traveltimes and amplitudes. This provides a first order diagnosis for regional trends. We then performed sub-regional 1-D (depth-dependent) waveform inversions for V_S and Q structure.

We used the direct solution method (DSM; Geller & Ohminato 1994; Kawai *et al.* 2006) for the forward modelling and convolved the synthetics with source-time functions estimated from the data set (see Appendix A). All the synthetics and observed data were sampled to 20 Hz and filtered between 0.005 and 0.08 Hz (i.e. for the period range 12.5–200 s).

We measured relative traveltimes and amplitudes by comparing observed and synthetic waveforms. Traveltimes and amplitudes can either be handpicked or measured with cross-correlation (e.g. Dahlen & Tromp 1998; Maggi *et al.* 2009). Here, we automatically pick the negative and positive peaks of both S and ScS wavelets independently. Thence, we define the traveltime as the midpoint time of the negative and positive wavelet peaks, and the amplitude as a difference between the two peaks (see Fig. 2). Note that this method is rapid and appropriate for the data set we used, since waveforms filtered up to 0.08 Hz have simple shapes, and that the results obtained by handpicking or cross-correlation methods lead to similar values. We do not use these values for inversions, but only for the characterization of our data set. Hence, the choice of traveltime and amplitude measurement methods is arbitrary here, and will not affect our final results.

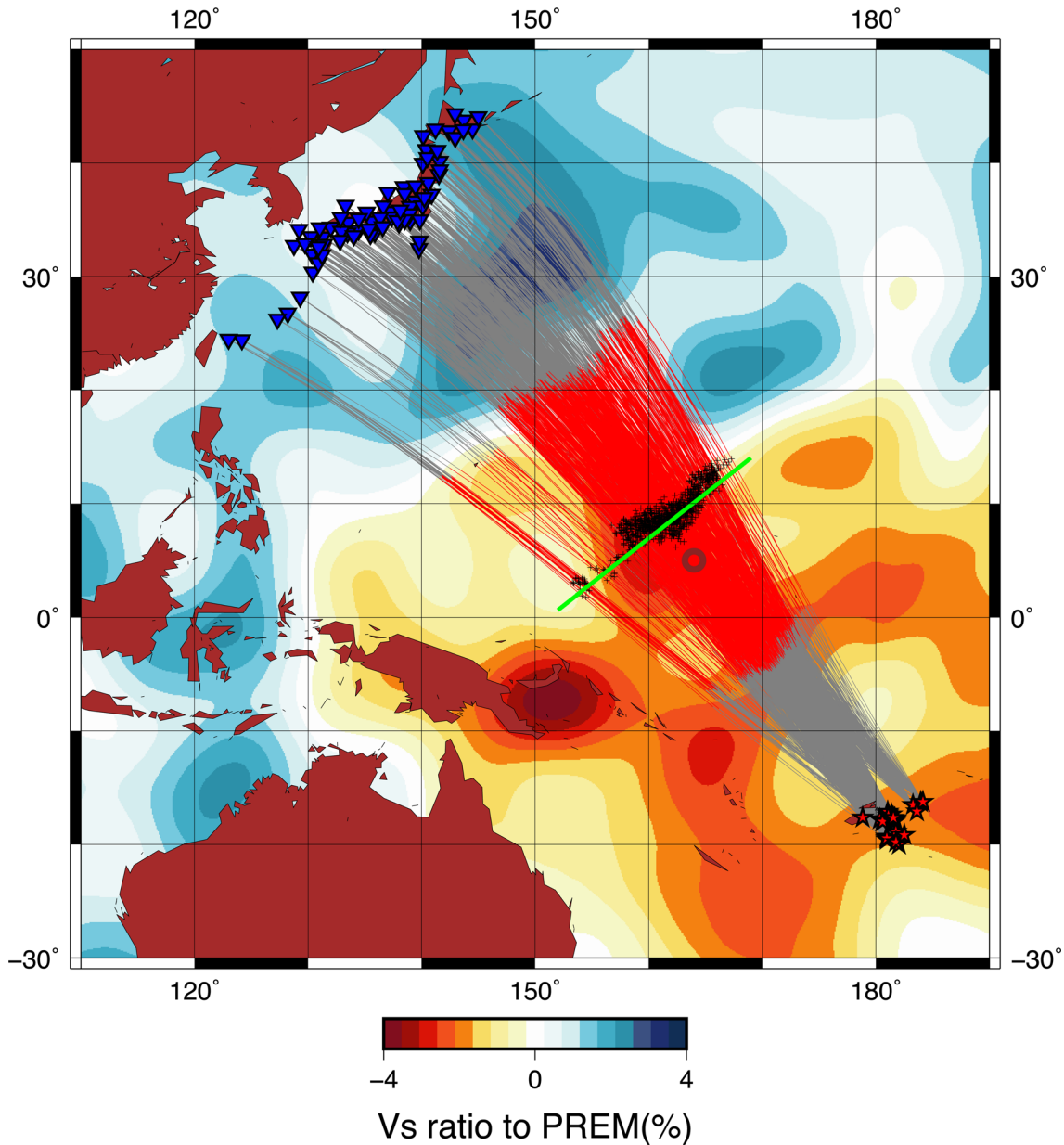


Figure 1. Geometrical distribution of seismic event (red stars) and stations (blue triangles) with great circle ray paths (grey curves). Bounce points of the ray paths are indicated by the crosses, and the regression line of these points indicated by the green line. The thick dark red circle indicates the location of the Caroline plume. The background colour shows the V_S model SEMUCB-WM1 (French & Romanovicz 2015) at a depth of 2800 km.

Fig. 3 shows traveltime residuals and amplitude ratios of S and ScS between observed and synthetic. Different symbols denote different events, and we plot all four observables as a function of epicentral distance. From Figs 3(a) and (c), it is clear that overall traveltime residuals are not evenly distributed around 0 s. Instead, S and ScS waves have average traveltime residuals of +0.40 s and +2.8 s, respectively, that is, observed data are slower than the synthetics. This observation indicates that V_S is slower than PREM' in this region, especially in the region sampled by the ScS phase, in the vicinity of the CMB. Looking at amplitude ratios (Figs 3b and d), the S phase has an average value of 1.0 whereas ScS phase shows an average of 0.68. This may be related to the presence of local scatterers (e.g. due to small scale changes in composition) or strong apparent attenuation in the vicinity of the CMB, compared to PREM'.

To investigate relative behaviours of these observables, in order that we can focus on the base of mantle, we also plotted differences between the observed and synthetic relative traveltime residuals, $\Delta t_{\text{obs}} - \Delta t_{\text{syn}}$, where $\Delta t = t_{ScS} - t_S$, and ratios of the observed and synthetic amplitude ratios of ScS and S , $R_{\text{obs}}/R_{\text{syn}}$, where $R = A_{ScS}/A_S$ (Fig. 4). Plots (c) and (d) in Fig. 4 further compare the differences in traveltime differences and amplitude ratios obtained with model PREM (black symbols) and PREM' (red symbols). Clearly, traveltimes are closer to the reference value (i.e. 0 for traveltime difference and 1 for amplitude ratio) in PREM' than in PREM, suggesting that PREM' is a much better model than PREM for this region. The differential traveltimes also indicate that we need a much slower model at the base of the mantle than PREM' for the data set of epicentral distances around 70°, and a moderately faster model (but still slower than PREM') for the data set of epicentral

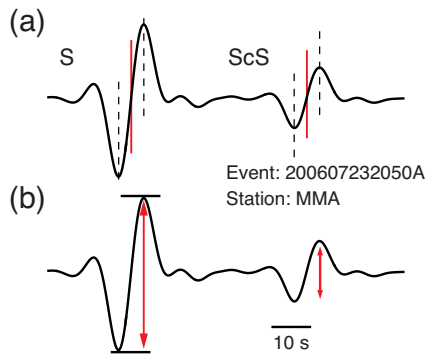


Figure 2. Time (a) and amplitude (b) quantitative comparison between observed and synthetic waveform. (a) Time comparison is based on the time of middle point between the lower and upper peaks of S and ScS waves. (b) Amplitude comparison is based on the peak-to-peak height of S and ScS phases.

distances around 75° . Note that here, we only show the values within the range from -5 to 10 s. Looking at differential amplitude of ScS , the data set of epicentral distances around 70° suggests very high attenuation and some moderately higher attenuation for the data set of epicentral distances around 75° . Based on the observation that the average values (over all seismic stations) of the traveltime residuals and amplitude ratios for a given seismic event do not significantly depend on the location of this event (Fig. 5), we assume that the differences we observe correspond to difference between the seismic structure (PREM') and the real Earth. In addition, the differences between the S and ScS phases are still large so that they may result mainly from anomaly in the lowermost part.

In order to identify possible ray path dependence of the anomalies in attenuation and V_S , we project the difference in traveltimes and amplitude ratios of each waveform on each bounce point of the ScS wave (Fig. 6). We observe large differences in both traveltimes ($ScS-S$) and amplitude ratios (ScS/S) at the centre of this region.

Fig. 7 shows the traveltime residuals and amplitude ratios projected on the regression line of the bounce points (green line in Fig 1), which is computed assuming that the relationship between latitudes and longitudes of the bounce points is linear. The data for the ray paths having a bounce point located in the centre (coloured in green) show larger traveltime residuals and smaller amplitude ratio than those on both sides (coloured in red and blue). Based on this observation, we separated our initial data set into three parts (labelled #1 to #3; Figs 7 and 8a). For each of three subdata set, we then conduct waveform inversion (detailed in Section 3) for quasi 2-D structures in the lowermost mantle beneath the western Pacific. The choice of the exact limits between each data set is subjective. Here, we separated the data set so that the ray paths of the subdata set #2 travel through the Caroline plume. Interestingly, the gradient of both traveltime residuals and amplitude ratios along the regression line is very smooth, suggesting that small differences in the limits between subdata sets have a limited impact. To check this point, we conducted additional inversions in which we slightly modified the limits between the subdata sets, but did not find significant changes in the output 1-D models of V_S and Q .

Hereinafter, we introduce the waveform residual $\delta\mathbf{d}$, in order to prepare the waveform inversion methodology description in the following section. This residual is defined by

$$\delta\mathbf{d} = \mathbf{d} - \mathbf{u} \quad (1)$$

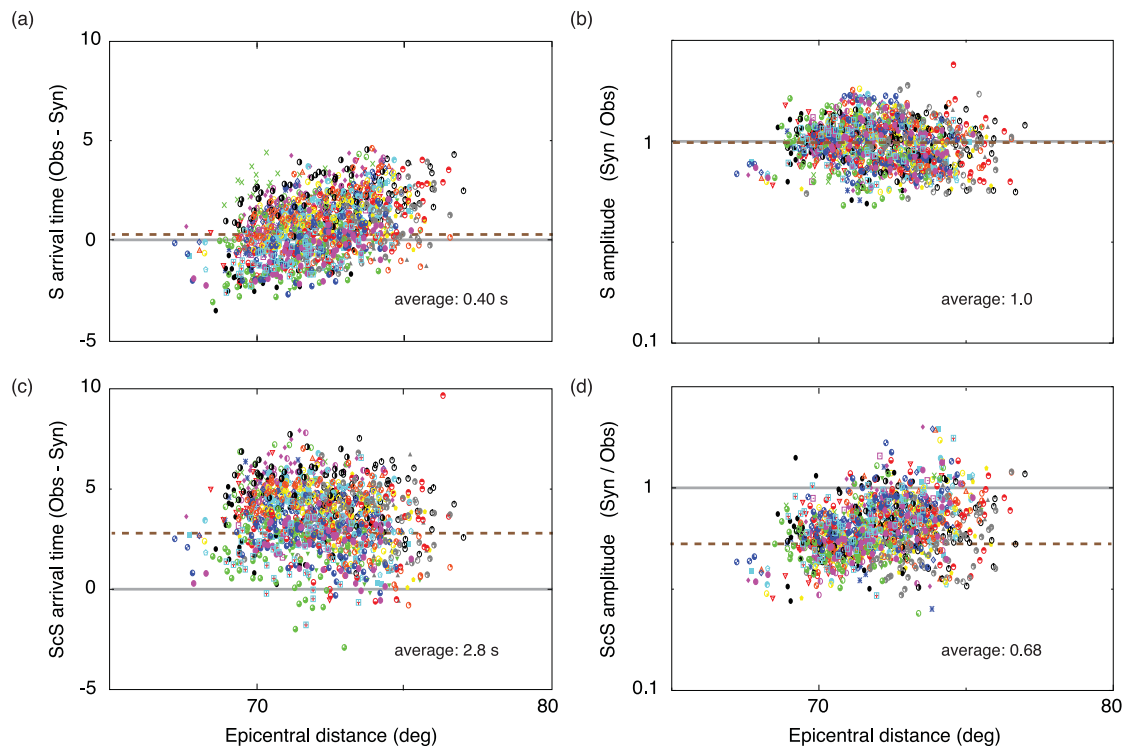


Figure 3. Differences between observed and synthetic waveforms. Each symbol shows the measurement for one seismic event. The traveltime residual (Fig. 2a) of each phase (S and ScS) is the difference between the arrival time for an observed and synthetic waveform (observed – synthetic). Amplitude measurement is the ratio between the synthetic and observed amplitudes (synthetic / observed) (Fig. 2b). (a) Traveltime residuals of S wave. (b) Amplitude measurement of S wave. (c) Traveltime residuals of ScS wave. (d) Amplitude measurement of ScS wave. The reference line is shown in grey and the brown dotted line shows each average value. Note that amplitude measurements are shown on a logarithmic scale.

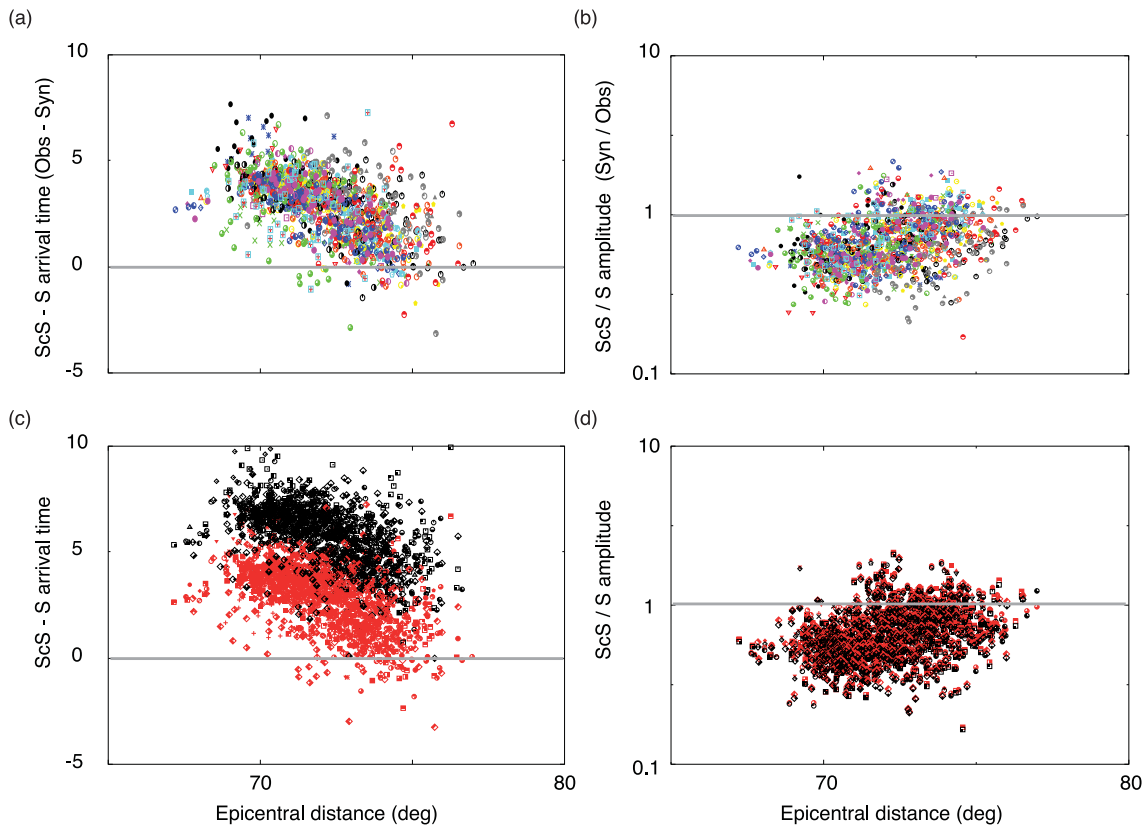


Figure 4. Relative difference in traveltime $\Delta t = (t_{ScS} - t_S)$ and amplitude ratio $R = A_{ScS}/A_S$ between observed and synthetic waveforms. (a) Difference between the observed and synthetic difference in traveltime ($\Delta t_{obs} - \Delta t_{syn}$), (b) Ratio of observed and synthetic amplitude ratios in ScS and S waves, R_{obs}/R_{syn} . Synthetics for (a) and (b) are computed for PREM'. The values obtained with PREM are also shown in (c) and (d) by black points, while the red points show the values for PREM'. Note that amplitude measurements (plots b and d) are shown on a logarithmic scale. The reference line is shown in grey.

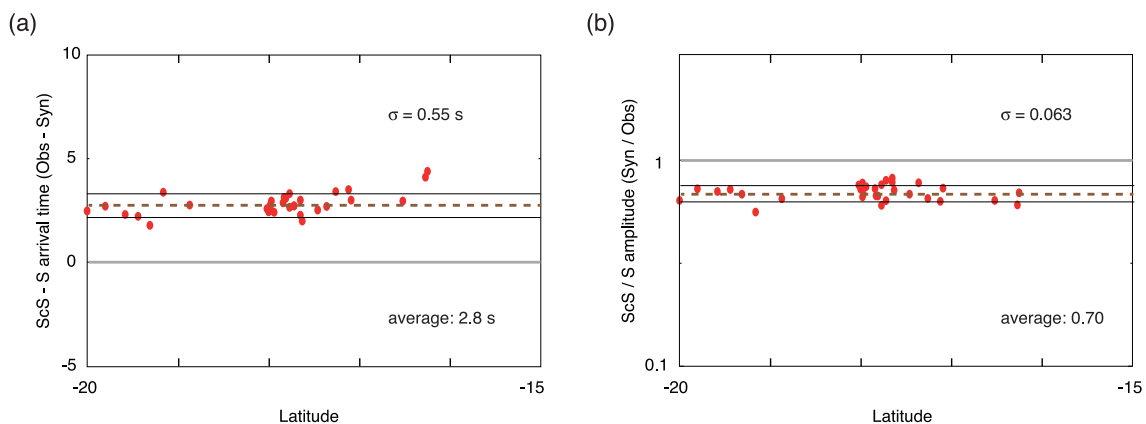


Figure 5. Average values of traveltime residuals (a) and amplitude ratios (b) of each event. Vertical axis indicates the traveltime residuals and amplitude ratios, and horizontal axis indicates the latitude for each event. The reference line is shown in grey, the brown dotted line shows each average value, and the thin line shows the value of the average $\pm 1\sigma$.

with \mathbf{d} and \mathbf{u} being the gathered waveform data points of observed and synthetic data computed for the initial model \mathbf{m} , respectively. The numbers of waveforms and relative residual variance between observed and synthetic waveforms are shown in Table 2, where the relative residual variance V is defined by

$$V(\mathbf{m}) = \frac{|\delta\mathbf{d}|^2}{|\mathbf{d}|^2}. \quad (2)$$

3 WAVEFORM INVERSION

In this section, we describe the simultaneous 1-D waveform inversion method for elastic and anelastic structure. This method is designed to minimize ℓ_2 -norm waveform misfit defined as follows:

$$E(\mathbf{m}) = \frac{1}{2} \delta\mathbf{d}^T \delta\mathbf{d}. \quad (3)$$

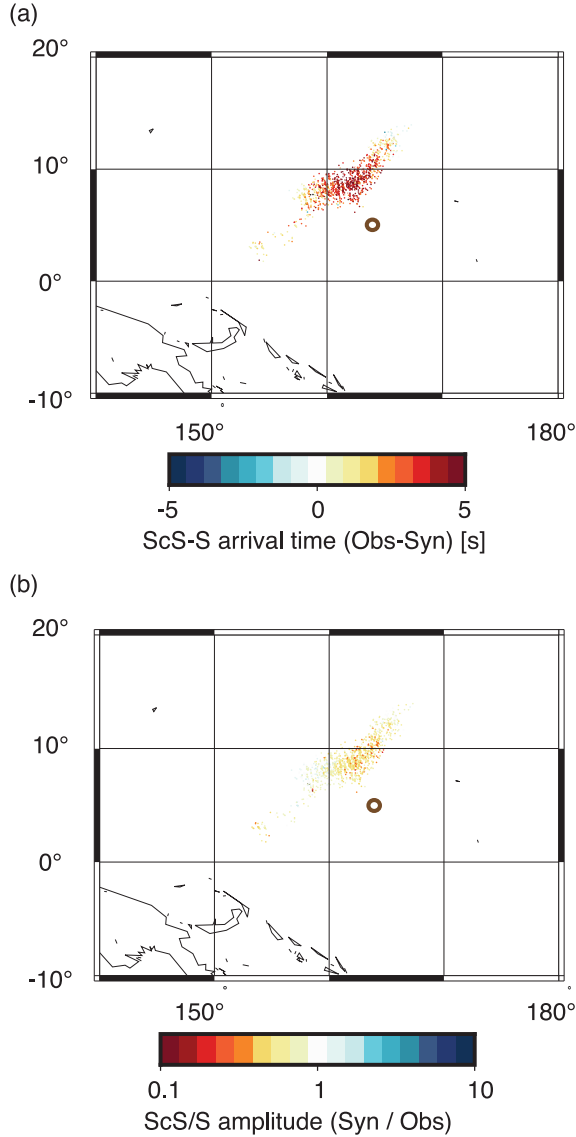


Figure 6. Relative difference in traveltime and amplitude between observed waveforms and PREM' projected at the bounce points of each ray path. (a) Traveltime residuals, (b) Amplitude ratios. The dark brown circles show the estimated location of the Caroline plume.

3.1 Inverse problem

Newton methods are derived by considering a Taylor expansion (e.g. Bertsekas 1982; Tarantola 1987; Pratt *et al.* 1998) with perturbations to the initial model $\delta\mathbf{m}$:

$$E(\mathbf{m} + \delta\mathbf{m}) = E(\mathbf{m}) + [\nabla_{\mathbf{m}} E(\mathbf{m})]^T \delta\mathbf{m} + \frac{1}{2} \delta\mathbf{m}^T [\nabla_{\mathbf{m}}^T [\nabla_{\mathbf{m}} E(\mathbf{m})]]^T \delta\mathbf{m} + \mathcal{O}(|\delta\mathbf{m}|^3). \quad (4)$$

The second term on the right-hand side of eq. (4) is the contribution from the gradient direction:

$$\nabla_{\mathbf{m}} E(\mathbf{m}) = -[\mathcal{D}_{\mathbf{m}} \mathbf{u}]^T \delta\mathbf{d}, \quad (5)$$

where $\mathcal{D}_{\mathbf{m}}$ denotes partial derivatives with respect to model parameters:

$$\mathcal{D}_{\mathbf{m}} \mathbf{u} = \frac{\partial \mathbf{u}}{\partial \mathbf{m}}. \quad (6)$$

The third term on the right-hand side of eq. (4) is the contribution from the Hessian second derivative matrix:

$$\begin{aligned} & \frac{1}{2} [\nabla_{\mathbf{m}}^T [\nabla_{\mathbf{m}} E(\mathbf{m})]] (= \nabla_{\mathbf{m}}^2 E(\mathbf{m})) \\ & = -[\mathcal{D}_{\mathbf{m}}^2 \mathbf{u}]^T \delta\mathbf{d} + [\mathcal{D}_{\mathbf{m}} \mathbf{u}]^T [\mathcal{D}_{\mathbf{m}} \mathbf{u}]. \end{aligned} \quad (7)$$

The first term on the right-hand side of eq. (7) is a secondary scattering effect, which is generally assumed to be negligible. We seek a vector $\delta\mathbf{m}$ that will locate the minimum within the quadratic approximation. For the linearized problem, this approach converges in one iteration, and the set of normal equations to be solved is

$$\mathbf{A}^T \mathbf{A} \delta\mathbf{m} = \mathbf{A}^T \delta\mathbf{d}, \quad (8)$$

where

$$\mathbf{A} = [\mathcal{D}_{\mathbf{m}} \mathbf{u}]. \quad (9)$$

The partial derivatives matrix \mathbf{A} consists of the number of data points times the number of unknown parameters. The diagonals of Hessian matrix $\mathbf{A}^T \mathbf{A}$ can be considered as a sensitivity kernel. In our case, the unknown parameters are set to be V_S and Q in the depth range of 2000–2891 km, with a vertical interval of 50 km. Since we are interested only in the structure of the lowermost mantle, we take a time window from the end of the direct S phase to the end of the ScS phase, normalizing both observed and synthetic data with respect to the amplitude of direct S phase of each source–receiver pair, and we align the direct S phase arrivals so that waveform inversion measures the differential traveltimes of ScS phases. Note that the values defined in Section 2 are used for the normalization and alignment. In order to solve eq. (8), we use the conjugate gradient (CG) method (Beckman 1960).

3.2 Partial derivatives

To calculate partial derivatives of the toroidal component of the displacement, u_T , with respect to the rigidity μ , we use the shell (or pixel) perturbation at radius r_Q for a seismogram at a receiver position \mathbf{r}_R with a source at position \mathbf{r}_S in the frequency domain (see general explanations in Geller & Hara 1993; Kawai & Geller 2010; Fuji *et al.* 2012):

$$\begin{aligned} & \frac{\partial u_T(\mathbf{r}_R, \omega; \mathbf{r}_S)}{\partial \mu(r_Q)} \delta\mu(r_Q, \omega) \\ & = -\epsilon_{\theta\phi}(r_Q, \omega; \mathbf{r}_S) \delta\mu(r_Q, \omega) h_{T\theta\phi}^*(r_Q, \omega; \mathbf{r}_R), \end{aligned} \quad (10)$$

where $\epsilon_{\theta\phi}$ denotes the lateral shear strain from the source to the perturbation, $h_{T\theta\phi}^*$ the back-propagated shear strain from the receiver to the source, and $\delta\mu(r_Q, \omega)$ the small perturbation to the starting model. Note that the rigidity μ is complex quantity, as is $\delta\mu$. For the expression of the integral calculating the partial derivative, $\frac{\partial u_T(\mathbf{r}_R, \omega; \mathbf{r}_S)}{\partial \mu(r_Q)}$, with respect to depth, we refer to eq. (4) of Kawai & Geller (2010). Fuji *et al.* (2010) write those frequency dependences by introducing $q = Q^{-1}$:

$$\mu(\omega) = \mu_0 \left(1 + \frac{2q \ln(\omega/\omega_0)}{\pi} \right) (1 + iq) \quad (11)$$

and

$$\begin{aligned} \delta\mu(\omega) & = \left(1 + \frac{2q \ln(\omega/\omega_0)}{\pi} \right) (1 + iq) \delta\mu_0 \\ & + \mu_0 \left[\frac{2 \ln(\omega/\omega_0)}{\pi} + i \left(1 + \frac{4q \ln(\omega/\omega_0)}{\pi} \right) \right] \delta q \end{aligned} \quad (12)$$

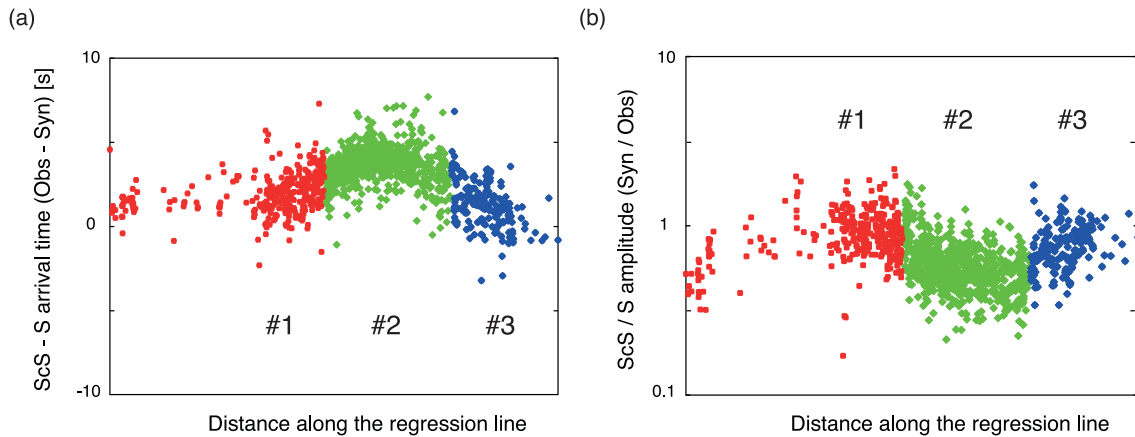


Figure 7. Traveltime residuals and amplitude ratios for each trace projected on the regression line (green line in Fig. 1). The vertical axis is the centre line and horizontal axis is (a) traveltime residuals, (b) amplitude ratios. The colour is used to distinguish the subdata sets (red for data set #1, green for data set #2 and blue for data set #3). The labels (#1 to #3) corresponds to the ones in Fig. 8.

where μ_0 denotes the value of the rigidity at a reference frequency, which is fixed to 1 Hz in our inversions.

3.3 Resolution check

To assess the vertical resolution of our V_S and Q models, we conducted checkerboard tests. For these tests, we defined four input models (black lines in Fig. 9), for which we calculate synthetic data sets. We then invert these synthetic data for output models with source–receiver configurations similar to those of the subdata set #2. The first test model (black lines in Figs 9a and b) is a standard checkerboard test with five layers in which V_S is alternatively faster and slower than PREM' by 1 per cent, and Q is alternatively equal to 350 and 250. Output models (red lines) for this test indicate that V_S is well resolved at depths larger than 2500 km, and that it is affected by slight trade-off at shallower depths. For Q , the output model suggests trade-offs throughout the depth range 2000–2850 km, but again, the Q structure is overall well recovered. The three other input V_S and Q models are simplified versions of the models obtained from real data (Section 4), and are thus specifically designed to check whether the anomalies we observe are well resolved. In the second and third test (Figs 9c and d, and e and f), we imposed either the V_S or the Q perturbations, the other parameter being set constant and equal to the PREM' value in all layers. Finally, in the fourth test (Figs 9g and h), the input model includes both V_S and Q perturbations. These tests indicate that the V_S structure is very well resolved throughout the depth range we explore, whereas the Q structure is affected by moderate trade-offs between 2000 and 2600 km. Overall, the input Q structure is well recovered, with deviations to the input profile being around 10 and less. Importantly, the lowermost part of our models, sampling the Pacific LLSVP, appears to be well resolved for both V_S and Q .

3.4 Sensitivity kernel

Fig. 10 shows diagonal values of Hessian matrix $\mathbf{A}^T\mathbf{A}$ for V_S and Q , respectively. As we conduct waveform inversion by the CG method, the $\mathbf{A}^T\mathbf{A}$ is expressed as $\mathbf{P}\mathbf{L}\mathbf{P}^T$ where

$$\mathbf{P} = (\mathbf{p}_1, \mathbf{p}_2, \dots, \mathbf{p}_M), \quad (13)$$

and

$$\mathbf{L} = \begin{pmatrix} \mathbf{p}_1\mathbf{A}^T\mathbf{A}\mathbf{p}_1 & & 0 \\ & \ddots & \\ 0 & & \mathbf{p}_M\mathbf{A}^T\mathbf{A}\mathbf{p}_M \end{pmatrix}. \quad (14)$$

Note that vectors \mathbf{p}_i are the CG vectors. Although we can see gradually increasing intensity of the values according to the depth, both sensitivity spreads well over our model space and there is no significant difference in the behaviour between the subregions.

4 SHEAR WAVE VELOCITY AND QUALITY FACTOR PROFILES

Obtained models of V_S and Q structure for the three regions are shown in Fig. 11. Clearly, the models for the data set #2 have lower values in both V_S and Q , compared to the models for the two other subregions, which are very similar with one another. This is consistent with the comparison of the traveltimes and amplitude ratios of the waveforms (Fig. 4). In the depth range 2000–2500 km, V_S models for data sets #1 and #3 are slightly slower (around 0.3–0.4 per cent) than PREM and Q is around 290, that is, smaller than the PREM value by about 7 per cent. In the depth range 2500–2800 km, V_S is again smaller than PREM, and the amplitude of the anomaly increases gradually from 1.7 per cent to 2.1–2.2 per cent, while Q decreases from 280 to 260, that is, smaller than PREM by 10 per cent and 17 per cent, respectively. The model for the data set #2 is slower than the other models by an additional 0.3 per cent throughout the depth range we explored, leading to anomalies (compared to PREM) around -0.6 per cent at 2000 km, and -2.4 per cent at 2850 km. This is consistent with the local variations in V_S observed by SEMUCB-WM1 (French & Romanowicz 2015) in this region. Note that at 2800 km, the minimum value in V_S in French & Romanowicz (2015) is slightly shifted to the west, compared to the position of the Caroline plume (Fig. 8), and that this minimum value in V_S is slightly slower, around 0.7 per cent, than the V_S we inferred for the data set #2. The V_S gradient is, however, similar, equivalent to a change of ~ 0.5 per cent for an angular distance of 10° . At 2000 km, the V_S found by French & Romanowicz (2015) are still slower by ~ 0.5 per cent than those seen in our models, but the contrast between the interior of the Caroline plume and its surrounding is, again, comparable to that between our model #2 and models #1 and #3. Similarly, in the region sampled by data set #2,

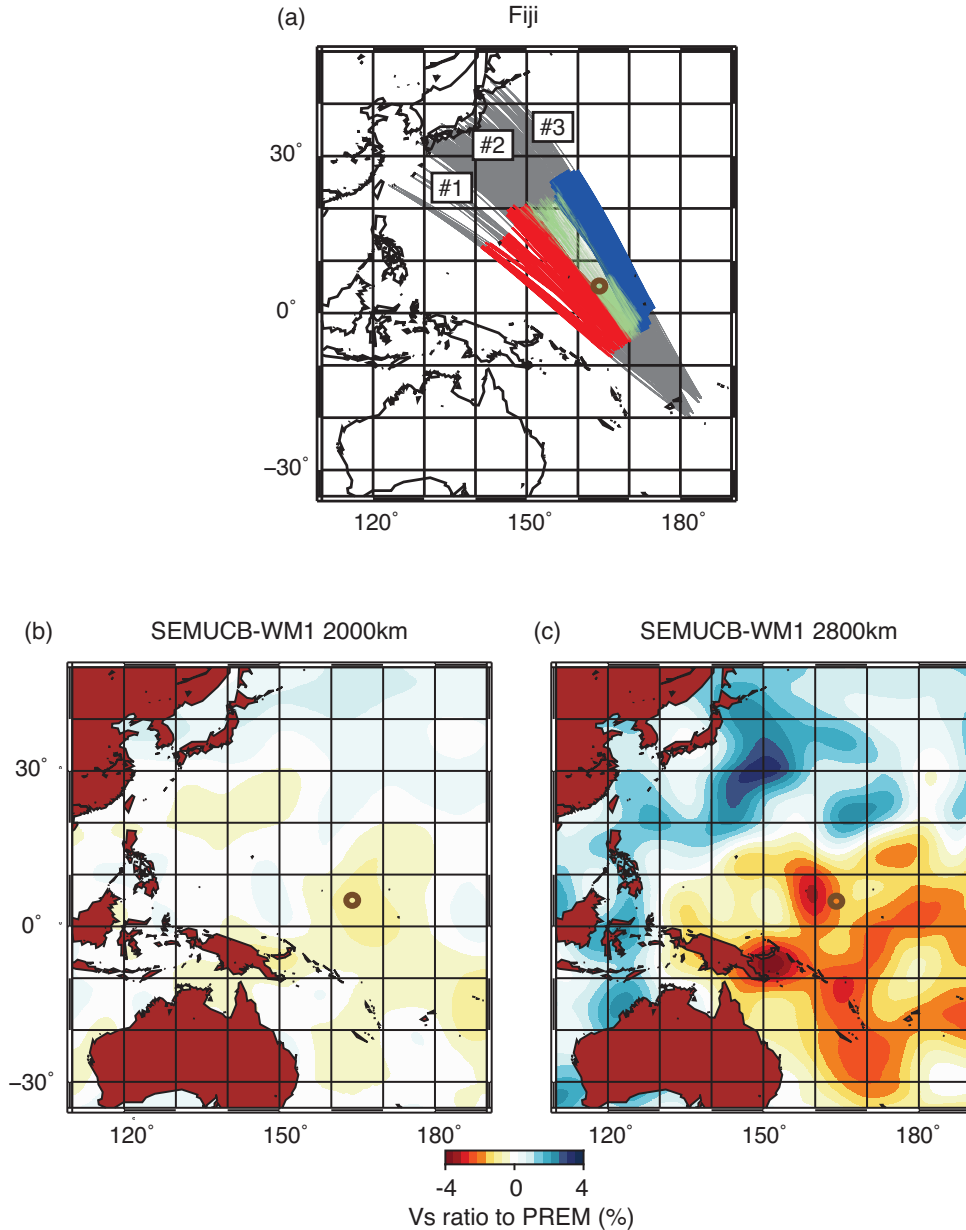


Figure 8. (a) Ray path bins divided in three parts. Labels 1, 2 and 3 are for the southern, central and northern paths, respectively. Coloured parts denote the parts of the ray paths travelling in the depth range 2000–2891 km. In plots (b) and (c), the background map shows the V_S model SEMUCB-WM1 (French & Romanovicz 2015) at depths of 2000 and 2800 km, respectively. The dark brown circles indicate the location of the Caroline plume.

Table 2. Number of waveforms and variance for each subdata set.

	Number of waveforms	$V(\mathbf{m})$ in eq. (2)
#1	337	0.96
#2	814	1.1
#3	190	0.75

Q is lower than in other regions, with values around 260 (17 per cent smaller than PREM) in the range 2000–2500 km, and down to 216 (31 per cent smaller than PREM) above the CMB. Relative anomalies in V_S with respect to PREM and values of Q at depths of 2000 and 2850 km are summarized in Table 3.

We do not see clear evidence for D'' discontinuity in our models. According to the resolution check (Section 3.3), we should be able

to see it, if it is there, and if it causes a large enough amplitude in V_S . However, resolution checks are ideal cases, and noise in the real data may degrade the resolution such that we do not see the signal of D'' . Generally speaking, the periods, and thus wavelengths, of the data used in this study are relatively too long to allow the detection of such a signal. In addition, the transition may exist but if it happens within a relatively wide depth range due to impurity of the composition, it may result in a gradual velocity change, in which case it would not induce a clear velocity discontinuity. Finally, it should be pointed out that, if related to the presence of post-perovskite (pPv), D'' might not be present in the region we explored, because this region may be too hot, and pPv would thus be unstable.

As discussed in Section 3.3, some trade-off between V_S and Q may exist. However, assuming that the amount of the trade-off is proportional to δV_S , the difference of Q between subdata set #2 and

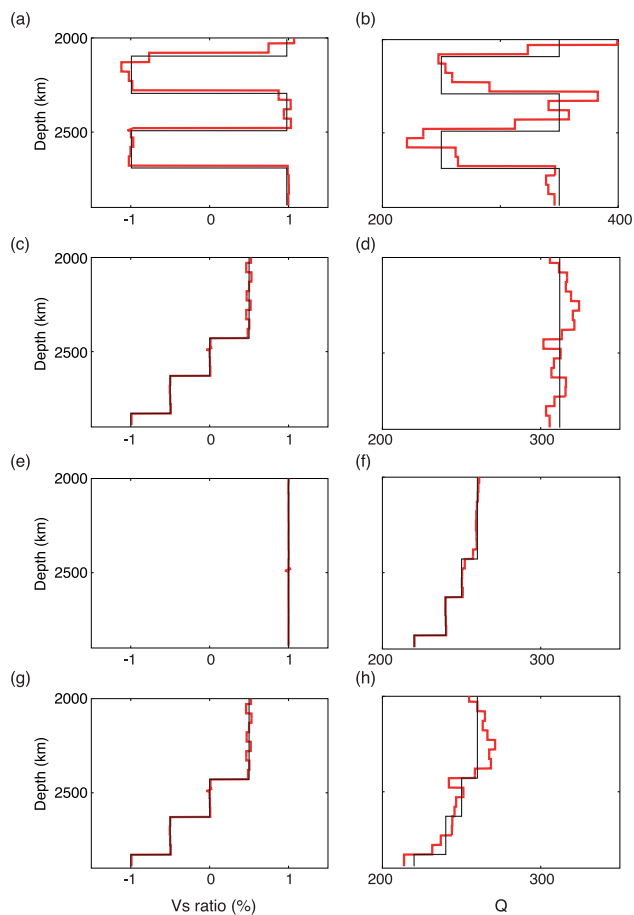


Figure 9. Checkerboard tests. Black and red lines are input and obtained models, respectively. Each horizontal set of two panels (i.e. ab, cd, ef and gh) is one test. Left and right panels show models of V_S anomalies and Q , respectively. The V_S model is shown in percentage to the initial model, that is, PREM'.

the others remains a few times larger than that of V_S , with a typical deviation around 10.

To further check the validity of the models we obtained, we performed comparisons between synthetic waveforms computed for the PREM' and the obtained models. Fig. 12 shows such comparisons for the data set #2 and #3. We stacked waveforms of near epicentral distances together, and aligned them according to ScS phase arrivals. Clearly, ScS peaks of stacked observed waveforms arrive later than synthetic waveforms computed by PREM' (Figs 12a and b). This suggests, as discussed in Section 2, that the difference of arrivals is larger for the paths of data set #2 than for those of data set #3. Figs 12(c) and (d) do not show substantial difference of arrivals anymore, suggesting that the obtained models would be a better model than PREM'. We also see larger differences in the arrivals for waveforms with smallest or largest epicentral distance, which may suggest more localized effects within each of the sub-region we defined. However, resolving these local features requires additional data and splitting our data set in smaller subsets.

Modification in traveltime residuals and amplitude ratios by the obtained models is shown in Fig. 13. Table 4 further shows the improvement in the variance reduction (the residual between the PREM' and the obtained models). Traveltimes and amplitude ratios apparently shift to values indicating unbiased models of 0 (for traveltime residuals) and 1 (for amplitude ratios), respectively, in all

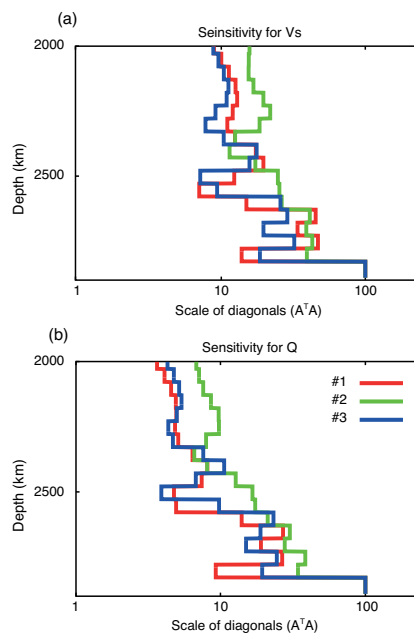


Figure 10. Sensitivity kernel for (a) V_S and (b) Q . Vertical axis shows depth. Horizontal axis indicates logarithm values of diagonal of $A^T A$ corresponding to a partial derivative for a given depth. All values are normalized by the value at the largest depth. Each colour represents each data set, red: #1, green: #2 and blue #3.

the data sets. Fig. 14 shows map view of traveltimes and amplitude ratios between observed waveforms and the obtained models for all the ray paths used in this study. Comparison with Fig. 6, clearly show improvements, with a general lack of features in both traveltimes and amplitude ratios, suggesting that there is very little signal left to extract from the data.

5 CONSTRAINTS ON TEMPERATURE ANOMALIES

Because both V_S and Q strongly depend on temperature, differences in the radial profiles at the different locations plotted in Fig. 11 may originate from lateral variations in temperature. V_S further depends on composition, in particular on the iron content, and may therefore reflect compositional effects due to the fact that LLSVPs may be enriched in iron oxide (Trampert *et al.* 2004; Deschamps *et al.* 2012; Mosca *et al.* 2012). The difference between model #2 and the other models (Table 3), sampling neighbouring regions, suggests that the region sampled by model #2 is warmer than the surrounding regions throughout the depth range we explored. Interestingly, a comparison with tomographic models (Takeuchi 2012; French & Romanowicz 2015) indicates that the region sampled by model #2 corresponds to the Caroline plume. Takeuchi & Obara (2010) also suggested the existence of anomalies in this region, which are usually interpreted as a thermal or thermochemical plume. Note that the lowermost parts of all models sample the Pacific LLSVP, which extends a few hundreds of kilometres above the CMB. Assuming that LLSVPs are chemically homogeneous, and independently of the fact that they may themselves be chemically distinct from the average mantle, our results suggest that temperature variations occur within the Pacific LLSVP. This hypothesis is consistent with global tomographic models (Ritsema *et al.* 2011; French & Romanowicz 2015), which map substantial lateral variations in V_S in the western tip of the Pacific LLSVP (Figs 1 and 8). At shallower depths, in the range

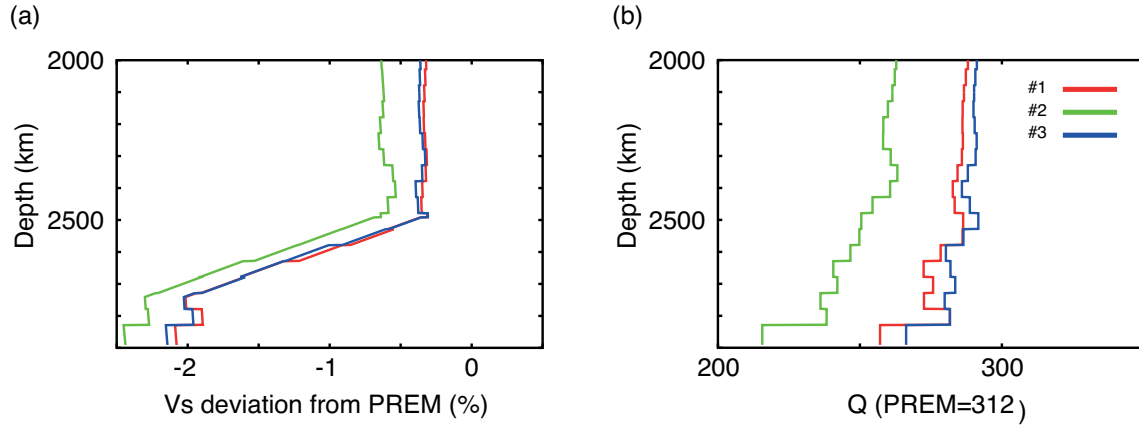


Figure 11. Results from waveform inversions. (a) and (b) panels show obtained models of V_S and Q . The velocity model is shown as per cent deviation from PREM. Each colour represents each data set, red: #1, green: #2 and blue: #3.

Table 3. V_S anomaly and Q -factor at location sampled by model #2, and in its surroundings (taken as the average between models #1 and #3, and labelled #1 for convenience). Note that the reference value for V_S is PREM.

Depth (km)	$d \ln V_S$		Q	
	#1	#2	#1	#2
2000	-0.35	-0.65	291	263
2850	-2.15	-2.45	261	216

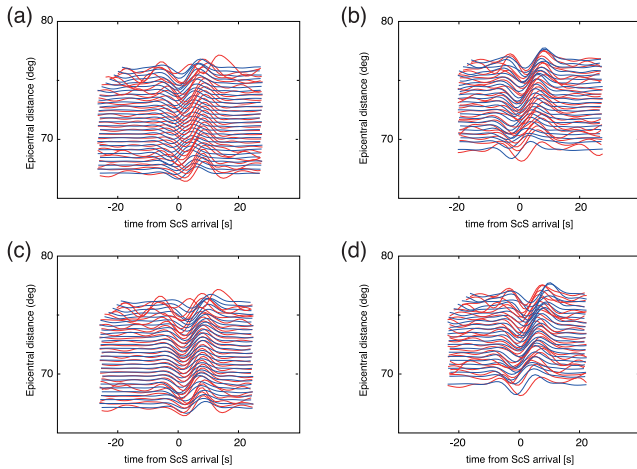


Figure 12. Observed (red) and synthetic (blue) stacked waveforms. (a,c) Waveforms in the data set #2. (b,d) Waveforms in the data set #3. Synthetics in panels (a) and (b) (top row) are computed for PREM' model and for the obtained models with the data set of #2 and #3, respectively, in panels (c) and (d) (bottom row).

2000–2500 km, the differences in V_S and Q we observe between region #2 and regions #1 and #3, may reflect difference in temperature (and possibly composition) between the inner part of the Caroline plume, and its edges or its surroundings. We now further quantify these temperature anomalies.

In the lowermost mantle (>2500 km) all our three models sample the western edge of the Pacific LLSVP. Assuming that, at this scale, the LLSVP is chemically homogeneous, differences in the profiles of V_S and Q at these depths should result from temperature variations only, and the temperature variations estimated with each of these two observables should be similar. At shallower depths, typically

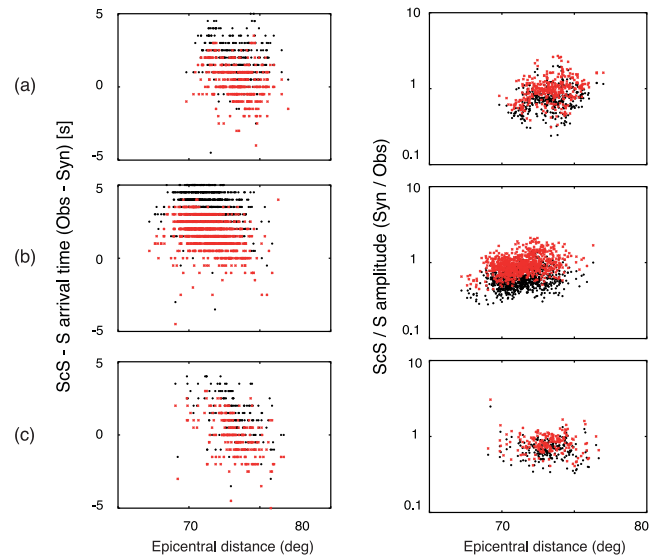


Figure 13. Traveltime residuals (left side panels) and amplitude ratios (right side panels) between observed and synthetic waveforms. The values for the PREM' and obtained model are in black (left) and red (right), respectively. The horizontal axis is epicentral distance between the seismic source and the station in each waveform. The vertical axes show the values of residuals and ratios. Each row shows the values for data sets (a) #1, (b) #2 and (c) #3.

Table 4. Improvement in the variance V (eq. 2) for each data set.

Improvement in variance (V)	
#1	0.18
#2	0.29
#3	0.13

2400 km and above, profiles do not any more sample the LLSVP, which culminates ~ 500 km above the CMB. In agreement with the helium isotopic ratio signature of Ocean Island Basalts (e.g. Allègre & Moreira 2004), numerical models of thermochemical convection indicate that thermal plumes rising from LLSVPs entrain small fractions of LLSVP material, around 10 per cent or less in volume (Deschamps *et al.* 2011). If, as discussed in Section 4, the central ray paths of our data set sample the Caroline plume, the V_S anomaly determined from the data set #2 would be slightly affected by the presence of a small excess of iron compared to its surroundings.

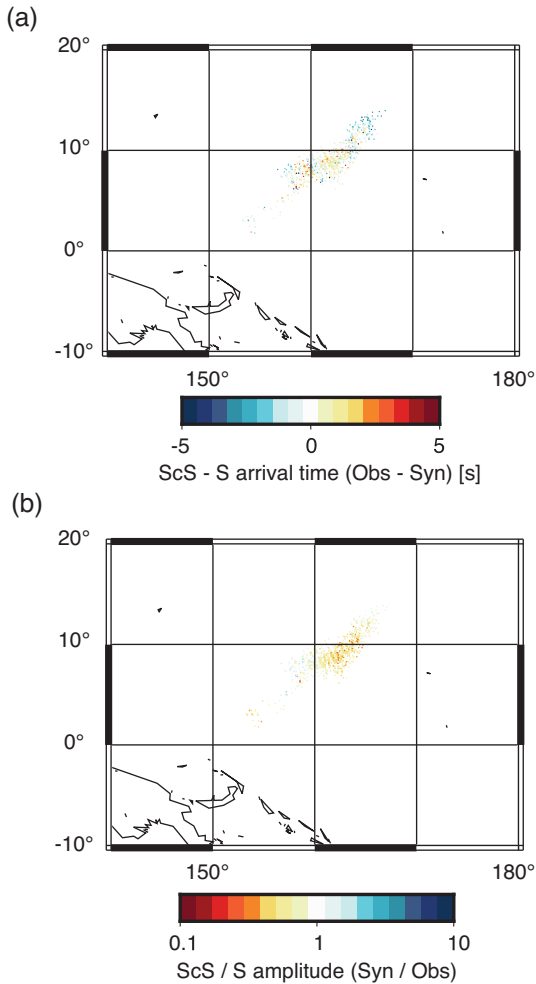


Figure 14. Same as Fig. 6, but for values obtained with the models of V_S and Q plotted in (Fig. 11).

Assuming that the Pacific LLSVP is enriched in iron by 3 per cent, compared to the average mantle, the plumes rising from it may be enriched in iron by 0.3 per cent.

Using the results plotted in Fig. 11, we calculated the temperature variations predicted by differences in V_S profiles and by differences in Q profiles. Temperature anomalies predicted by V_S anomalies are simply given by

$$dT_{V_S} = d \ln V_S / S_T, \quad (15)$$

where $d \ln V_S$ is the observed relative velocity anomaly between the profiles (with PREM taken as a reference value for V_S), and S_T is the sensitivity of V_S to temperature. If $d \ln V_S$ is affected by changes in the iron content, dT_{V_S} is then given by

$$dT_{V_S} = (d \ln V_S - S_{Fe} dX_{Fe}) / S_T, \quad (16)$$

where dX_{Fe} is the assumed anomaly in iron, and S_{Fe} is the sensitivity of V_S to iron. Here, we used sensitivities from Deschamps *et al.* (2012), which were calculated from a self-consistent mineral physics data set (Stixrude & Lithgow-Bertelloni 2011) and an equation of state modelling that accounts for uncertainties in both the thermoelastic properties of mantle minerals and the mantle reference thermochemical model (Cobden *et al.* 2012). These uncertainties allow the calculation of probability density functions

(rather than single values) for dT_{V_S} , from which uncertainties and ranges of likely values can be determined.

To calculate temperature anomalies predicted by differences in attenuation, we follow a classical modelling of the quality factor (for details, see e.g. Matas & Bukowinski 2007). If attenuation is small enough, the quality factor follows a power-law, with exponent α , of the frequency ω and of the characteristic relaxation time (Minster & Anderson 1981). Attenuation is a thermally activated process, and assuming that the relaxation time follows an Arrhenius law, the quality factor can be written as (e.g. Anderson & Given 1982)

$$Q = Q_0 \omega^\alpha \exp\left(\alpha \frac{H}{RT}\right), \quad (17)$$

where Q_0 is a constant, R the ideal gas constant, and $H = E + PV$ the activation enthalpy, with E and V being the activation energy and volume, respectively, and P the pressure. Possible values of the exponent α and the activation enthalpy have been discussed and modelled in Matas & Bukowinski (2007). In calculations below, we assumed $0.2 \leq \alpha \leq 0.4$. Note that the exact value of H may depend on the composition of the mantle aggregate composition, in particular on the respective fractions of bridgmanite and ferro-periclase. At a given depth, and following eq. (16), the relative anomaly in quality factor with respect to the reference value Q_{ref} (here taken as the PREM value, $Q_{ref} = 312$), $d \ln Q$, can be related to the temperature anomaly dT_Q with respect to a reference temperature T_{ref} (taken as the average mantle geotherm) by

$$d \ln Q = \frac{Q - Q_{ref}}{Q_{ref}} = \frac{1}{Q_{ref}} \left(\frac{\partial Q}{\partial T} \right)_{T=T_{ref}} dT_Q. \quad (18)$$

The temperature anomaly is therefore given by

$$dT_Q = \frac{-RT_{ref}^2}{\alpha H} d \ln Q. \quad (19)$$

The difference of temperature between two given locations is simply given by the difference in the temperature anomaly calculated at each of these two points. The differences predicted by variations in shear velocity and attenuation are then given by

$$\Delta T_{V_S} = [d \ln V_{S_2} - d \ln V_{S_1} - S_{Fe}(dX_{Fe_2} - dX_{Fe_1})] / S_T \quad (20)$$

and

$$\Delta T_Q = -\frac{RT_{ref}^2}{\alpha H} \frac{(Q_2 - Q_1)}{Q_{ref}} \quad (21)$$

where subscripts 1 and 2 denote the two given locations. We calculated the temperature difference between the region sampled by model #2 and the surrounding regions (models #1 and #3), using the values of Q and $d \ln V_S$ listed in Table 3.

Fig. 15 shows ΔT_{V_S} (horizontal bands) and ΔT_Q (curves) at depths of 2000 and 2850 km. For ΔT_{V_S} , the width of the bands is calculated from the range of seismic sensitivities bounded by the 0.15 and 0.85 quartiles (i.e. including 70 per cent of the explored sensitivities; Deschamps *et al.* 2012). For ΔT_Q , results are plotted as a function of H , and we considered three values of the reference temperature, T_{ref} , covering a conservative range of possible values. The median value of T_{ref} at 2850 km, 3750 K, corresponds to the upper bound of estimates based on the solidus of pyrolite (Nomura *et al.* 2014). Numerical models of thermochemical convection (Li *et al.* 2015) showed that a CMB temperature around this value explains lower mantle structures better than higher (>4000 K) and lower (<3400 K) values. The median value at 2000 km is estimated by adding an adiabatic temperature increase of 250 K to a super-adiabatic temperature jump in the layer 2000–2850 km,

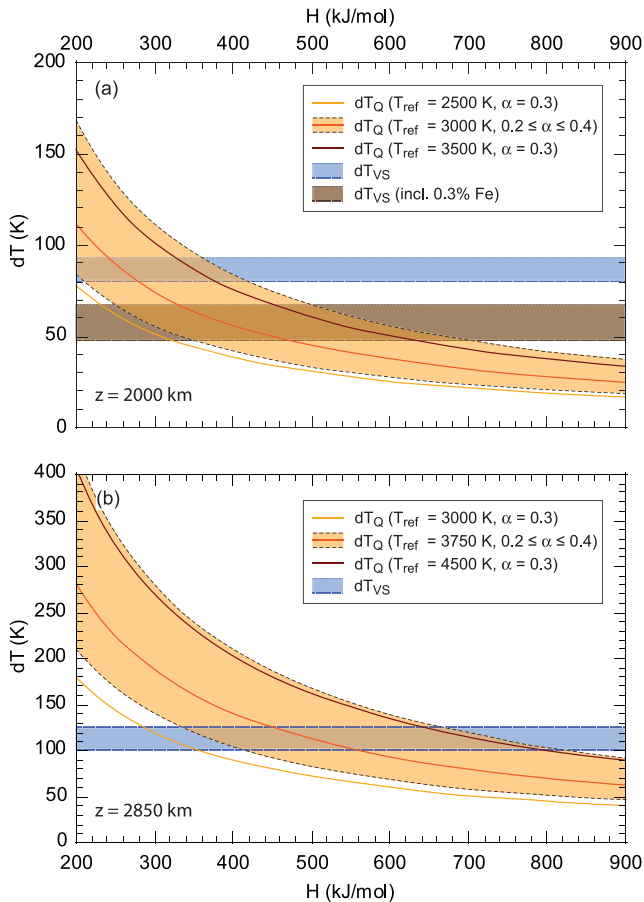


Figure 15. Temperature variations at 2000 km (a) and 2850 km (b) estimated from differences between model #2 and models #1 and #3 in Fig. 11. Temperature anomalies estimated from differences in the quality factor, dT_Q , are plotted as a function of the activation enthalpy (H), and for $\alpha = 0.3$ and several values of the reference temperature, T_{ref} (colour code). The orange shaded area around the curves for intermediate values of T_{ref} shows the effect of varying α in the range 0.2–0.4. Temperature anomalies estimated from differences in shear wave velocity, dT_{V_S} , are denoted by the horizontal shaded bands. Blue bands assume that the V_S difference is purely thermal, and the brown band at $z = 2000$ km assumes an additional excess of iron of 0.3 per cent (compared to surrounding mantle), due to the entrainment of LLSVP material by the Caroline plume.

which we fixed assuming that the temperature jump in the thermal boundary layer is comparable to the maximum amplitude in lateral temperature anomalies at the bottom of the mantle. This parameter remains poorly constrained, but may range between 400 K (Trampert *et al.* 2004; Mosca *et al.* 2012) and 750 K (Tackley 2012). Here, we fixed the superadiabatic jump to 500 K. This leads to a median temperature at 2000 km depth of 3000 K, which is on the hot side compared to adiabatic temperature profiles obtained for a potential temperature of 1600 K. The shaded area around the curves for the median values of T_{ref} represents the effect of varying α in the range 0.2–0.4. Assuming that the difference in shear wave velocity is entirely due to variations in temperature, dT_{V_S} is around 100–120 K at 2850 km, and drops to slightly lower values, 80–90 K, at 2000 km. If models #2 in Fig. 11 sample the Caroline plume, and if this plume is slightly enriched (by 0.3 per cent) in iron due to entrainment of LLSVP material, the temperature difference at 2000 km is even smaller, in the range 50–70 K. Small variations in iron within the Pacific LLSVP would also decrease the estimated

ΔT_{V_S} at 2850 km by a few tens of K, but again, we assumed here that the Pacific LLSVP is chemically homogeneous in this region, even if its composition differs from that of the surrounding mantle.

Excess of temperature in plumes is not well constrained. Estimates from petrological and isotope geochemistry constraints range between 160 and 280 K (Schilling 1991). Estimates based on geophysical observations, in particular topography, geoid, and heat flow are more uncertain and lead to temperature excess around 200 K in the asthenosphere (Sleep 1990). It has been pointed out that if plumes are originating from the CMB region, the temperature jump across the thermal boundary layer from which they rise should be relatively high, of the order of 1000 K (Jeanloz & Morris 1986), leading to large temperature excess within plumes tails. However, geodynamics studies showed that several parameters, including the presence of chemical reservoirs at the bottom of the mantle (Farnetani 1997), strongly reduce these values. For a layer denser than average mantle by 3 per cent, and assuming a temperature jump of 500 K in the thermal boundary layer, extrapolation of Farnetani (1997) models indicates that the excess temperature in a plume tail at 2000 km depth should be around 220 K. These estimates are somewhat higher than the temperature difference we inferred between the Caroline plume (sampled by data set #2) and its surroundings (sampled by data set #1 and #3). It should be reminded, however, that the petrological and geodynamics estimates of plume temperature excess are relative to the ambient mantle, i.e. to an average geotherm. Because V_S and Q in the regions sampled by data set #1 and #3 are smaller than the PREM values, these regions should be themselves hotter than the average mantle. Taking sensitivities of shear wave velocity to temperature and iron of Deschamps *et al.* (2012) within their error bars, a velocity anomaly of -0.65 per cent at 2000 km should result in a temperature anomaly (compared to average mantle) in the range 150–180 K if the plume is slightly enriched in iron, and 190–220 K if it is not. These values are consistent with petrological and geodynamics estimates.

The ranges of values of H , α , and T_{ref} we explored allow a wide agreement between our estimates of temperature difference based on attenuation (ΔT_Q) and on V_S anomalies (ΔT_{V_S}). At $z = 2850$ km, for $T_{\text{ref}} = 3750$ K and $\alpha = 0.3$, ΔT_Q fits within the estimated range of ΔT_{V_S} for values of H in the range 450–550 kJ mol⁻¹. At $z = 2000$ km, the range of H fitting the estimated ΔT_{V_S} drops to 240–280 kJ mol⁻¹ if variations in shear wave velocity are purely thermal in origin, and 340–480 kJ mol⁻¹ if they are due to the combination of temperature and iron (0.3 per cent excess) variations. Agreement between ΔT_Q and ΔT_{V_S} with larger values of T_{ref} and/or α requires larger values of H , and vice versa. Due to lack of constraints on T_{ref} , H , and α , it is, however, difficult to make finer and more discriminative comparisons. Interestingly, the fact that the values of H for which ΔT_Q agrees with ΔT_{V_S} are increasing with depth is consistent with the observation that for mantle materials the volume activation of attenuation (V) is positive, that is, H increases with pressure. According to the modelling of Matas & Bukowski (2007), H should increase by ~ 50 kJ mol⁻¹ between 2000 km depth and the CMB. If correct, this estimate would favour the hypothesis that the Caroline plume entrains a small fraction of iron-rich LLSVP material, since it requires a smaller increase in H between 2000 and 2850 km (Fig. 15).

Our calculations implicitly assume that Q does not significantly depend on the composition, and in particular on the iron content. The sensitivity of Q to composition is difficult to estimate, since it may affect all parameters in eq. (16), Q_0 , α , and H , and that there are very few mineral physics constraints on these parameters for the lower mantle minerals. Assuming, that mostly H is affected

by composition, it is possible to estimate its influence on Q . The relative variation in Q due to temperature variation dT is given by

$$(d \ln Q)_T = -\frac{\alpha H}{RT^2} dT. \quad (22)$$

Similar variation due to a variation in activation energy dH is given by

$$(d \ln Q)_H = \frac{\alpha}{RT} dH. \quad (23)$$

Equating these two relationships indicates that a relative change in temperature, dT/T , leads to a change in Q similar to the change induced by a relative change in H , dH/H . For instance, taking $H = 500 \text{ kJ mol}^{-1}$ and $T = 3750 \text{ K}$, a variation in temperature of 100 K is equivalent to a change in H of about 13 kJ mol^{-1} .

6 CONCLUSIONS AND PERSPECTIVES

In this study, we obtained 1-D radial models of shear wave velocity (V_S) and seismic attenuation (Q) at the base of the mantle for three distinct locations beneath the western Pacific, one of which matches the Caroline plume as imaged by tomographic models (French & Romanowicz 2015). The models built for the central region, corresponding to the Caroline plume, show lower values in both V_S and Q . At depths shallower than 2500 km , these anomalies may reflect temperature anomalies between the interior of the Caroline plume and its edges or its surroundings. Small amounts of iron rich material originating from the Pacific LLSVP and entrained by the plume may contribute to the seismic anomaly observed in the plume region. At greater depths, our results suggest that temperature variations occur within the Pacific LLSVP.

A possible extension of this work is to use jointly V_S and Q anomalies to resolve the thermal and compositional contributions to seismic anomalies. Assuming a sensitivity of V_S to temperature, S_T , equal to $-2.4 \times 10^{-5} \text{ K}^{-1}$ (Deschamps *et al.* 2012) and a V_S anomaly of 2.4 per cent (Table 3), eq. (15) indicates that if the Pacific LLSVP is not enriched in iron compared to surroundings ($dX_{\text{Fe}} = 0$) the excess of temperature (compared to average mantle) in the region sampled by our subdata set #2, should be around 1000 K . This value is very difficult to reconcile with temperature anomalies estimated from attenuation (eq. 18). For instance, taking $T_{\text{ref}} = 3750 \text{ K}$, $\alpha = 0.3$, $H = 400 \text{ kJ mol}^{-1}$ and $Q_{\text{PREM}} = 312$, the temperature excess corresponding to $Q = 216$ is around 300 K . A temperature excess of 1000 K would require the combination of a very large lowermost mantle reference (average) temperature ($>4500 \text{ K}$), and small values of α (<0.2) and activation enthalpy ($<200 \text{ kJ mol}^{-1}$), which are all unlikely (Matas & Bukowinski 2007; Nomura *et al.* 2014; Li *et al.* 2015). This disagreement suggests two conclusions. First, in the lowermost mantle, Q seems to be more sensitive to temperature than to composition, whereas V_S is strongly sensitive to both temperature and composition (in particular iron content). Second, explaining simultaneously our 1-D models of V_S and Q in the western edge of the Pacific LLSVP requires that this region is enriched in iron, compared to the ambient mantle. This point, however, needs to be investigated more in details since other parameters, including the presence of post-perovskite around the Pacific LLSVP, may also play a role in explaining the V_S and Q structures that we observe.

In order to simply explain the unique structure for the centre paths, the characteristics of the plume may be very thin and localized, otherwise, the plume would show large internal heterogeneities. If the Caroline plume is composed of small, hot plumes aggregated together, as suggested in Konishi *et al.* (2014), 3-D het-

erogeneities in the Q structure should also be present. It is further interesting to note that our model still suggests that anomalies in traveltimes are present at the centre of the target region, as mentioned in Section 4. These may be resolved by conducting 3-D waveform inversions. The fact that we used linear approximations to formulate waveform inversion for obtaining V_S and Q models requires that the initial model should be close enough to the real structure. Even if massive data sets improve resolution, non-linear effects may induce substantial bias and errors. This difficulty may be solved by first obtaining a first-order model as accurate as possible with an approach that is not affected by non-linearity. Finally, thanks to the increase in computational power, 3-D waveform inversions may be conducted using Monte-Carlo methods, which would allow estimates of uncertainties in shear wave velocity and attenuation.

ACKNOWLEDGEMENTS

We are grateful to Laura Cobden and an anonymous reviewer for their detailed and constructive reviews that helped improving a first version of this article. This study was supported by Academia Sinica Career Development Award 102-CDA-M02. We acknowledge NIED (National Research Institute for Earth Science and Disaster Prevention, Japan) for providing us the F-net data, and Martin Vallée for providing SCARDEC source time function database.

REFERENCES

- Allègre, C.J. & Moreira, M., 2004. Rare gas systematic and the origin of oceanic islands: the key role of entrainment at the 670 km boundary layer, *Earth planet. Sci. Lett.*, **228**, 85–92.
- Anderson, D.L. & Given, J.W., 1982. Absorption band Q model for the Earth, *J. geophys. Res.*, **87**, 3893–3904.
- Beckman, F.S., 1960. The solution of linear equations by the conjugate gradient method, in *Mathematical Methods for Digital Computers*, eds Ralston, A. & Wilf, H.S., Wiley.
- Bertsekas, D.P., 1982. *Constrained Optimization and Lagrange Multiplier Methods*, Academic Press.
- Cobden, L., Mosca, I., Trampert, J. & Ritsema, J., 2012. On the likelihood of post-perovskite near the core-mantle boundary: a statistical interpretation of seismic observations, *Phys. Earth planet. Inter.*, **210–211**, 21–35.
- Dahlen, F.A. & Tromp, J., 1998. *Theoretical Global Seismology*, Princeton Univ. Press.
- Davies, D.R., Goes, S. & Lau, H.C.P., 2015. Thermally dominated deep mantle LLSVPs: a review, in *The Earth's Heterogeneous Mantle*, Springer Geophysics, pp. 441–477, eds Khan, A. & Deschamps, F., Springer International Publishing.
- Deschamps, F., Kaminski, E. & Tackley, P.J., 2011. A deep mantle origin for the primitive signature of Ocean Island Basalt, *Nat. Geosci.*, **4**, 879–882.
- Deschamps, F., Cobden, L. & Tackley, P.J., 2012. The primitive nature of large low shear-wave velocity provinces, *Earth planet. Sci. Lett.*, **349–350**, 198–208.
- Deschamps, F., Li, Y. & Tackley, P.J., 2015. Large-scale thermo-chemical structure of the deep mantle: observations and models, in *The Earth's Heterogeneous Mantle*, Springer Geophysics, pp. 479–515, eds Khan, A. & Deschamps, F., Springer International Publishing.
- Dziewonski, A.M. & Anderson, D.L., 1981. Preliminary reference earth model, *Phys. Earth planet. Inter.*, **25**, 297–356.
- Farnetani, C.G., 1997. Excess temperature of mantle plumes: the role of the chemical stratification across D'' , *Geophys. Res. Lett.*, **24**, 1583–1586.
- French, S.W. & Romanowicz, B., 2015. Broad plumes rooted at the base of the Earth's mantle beneath major hotspots, *Nature*, **525**, 95–99.
- Fuji, N., Kawai, K. & Geller, R.J., 2010. A methodology for inversion of broadband seismic waveforms for elastic and anelastic structure and its application to the mantle transition zone beneath the northwestern Pacific, *Phys. Earth planet. Inter.*, **180**, 118–137.

- Fuji, N., Chevrot, S., Geller, R.J. & Kawai, K., 2012. Finite-frequency structural sensitivities of short-period compressional body waves, *Geophys. J. Int.*, **190**, 522–540.
- Garnero, E.J., McNamara, A.K. & Shim, S.-H.D., 2016. Continent-sized low seismic velocity anomalies at the base of Earth's mantle, *Nat. Geosci.*, **9**, 481–489.
- Geller, R.J. & Hara, T., 1993. Two efficient algorithms for iterative linearized inversion of seismic waveform data, *Geophys. J. Int.*, **115**, 699–710.
- Geller, R.J. & Ohminato, T., 1994. Computation of synthetic seismograms and their partial derivatives for heterogeneous media with arbitrary natural boundary conditions using the direct solution method, *Geophys. J. Int.*, **116**, 421–446.
- He, Y. & Wen, L., 2009. Structural features and shear-velocity structure of the “Pacific Anomaly”, *J. geophys. Res.*, **114**, B02309, doi:10.1029/2008JB005814.
- Houser, C., Masters, G., Shearer, P. & Laske, G., 2008. Shear and compressional velocity models of the mantle from cluster analysis of long-period waveforms, *Geophys. J. Int.*, **174**, 195–212.
- Ishii, M. & Tromp, J., 1999. Normal-mode and free-air gravity constraints on lateral variations in velocity and density of Earth's mantle, *Science*, **285**, 1231–1236.
- Jeanloz, R. & Morris, S., 1986. Temperature distribution in the crust and mantle, *Annu. Rev. Earth Planet. Sci.*, **14**, 377–415.
- Kawai, K. & Geller, R.J., 2010. Waveform inversion for localized seismic structure and an application to D'' structure beneath the Pacific, *J. geophys. Res.*, **115**, B01305, doi:10.1029/2009JB006503.
- Kawai, K., Takeuchi, N. & Geller, R.J., 2006. Complete synthetic seismograms up to 2 Hz for transversely isotropic spherically symmetric media, *Geophys. J. Int.*, **164**, 411–424.
- Konishi, K., Kawai, K., Geller, R.J. & Fuji, N., 2009. MORB in the lowermost mantle beneath the western pacific: evidence from waveform inversion, *Earth planet. Sci. Lett.*, **278**, 219–225.
- Konishi, K., Kawai, K., Geller, R.J. & Fuji, N., 2014. Waveform inversion for localized three-dimensional seismic velocity structure in the lowermost mantle beneath the western pacific, *Geophys. J. Int.*, **199**, 1245–1267.
- Kustowski, B., Ekström, G. & Dziewonski, A.M., 2008. Anisotropic shear-wave velocity structure of the Earth's mantle: a global model, *J. geophys. Res.*, **113**, B06306, doi:10.1029/2007JB005169.
- Li, Y., Deschamps, F. & Tackley, P.J., 2015. Effects of the post-perovskite phase transition properties on the stability and structure of primordial reservoirs in the lower mantle of the Earth, *Earth planet. Sci. Lett.*, **432**, 1–12.
- Maggi, A., Tape, C., Chen, M., Chao, D. & Tromp, J., 2009. An automated time-window selection algorithm for seismic tomography, *Geophys. J. Int.*, **178**, 257–281.
- Matas, J. & Bukowski, M.S.T., 2007. On the anelastic contribution to the temperature dependence of lower mantle seismic velocities, *Earth planet. Sci. Lett.*, **259**, 51–65.
- Minster, B. & Anderson, D.L., 1981. A model of dislocation-controlled rheology for the mantle, *Phil. Trans. R. Soc. A*, **299**, 319–356.
- Mosca, I., Cobden, L., Deuss, A., Ritsema, J. & Trampert, J., 2012. Seismic and mineralogical structures of the lower mantle from probabilistic tomography, *J. geophys. Res.*, **117**, B06304, doi:10.1029/2011JB008851.
- Ni, S., Tan, E., Gurnis, M. & HelMBERGER, D., 2002. Sharp sides to the African superplumes, *Science*, **296**, 1850–1852.
- Nomura, R., Hirose, K., Uesugi, K., Ohishi, Y., Tsuchiyama, A., Miyake, A. & Ueno, Y., 2014. Low core–mantle boundary temperature inferred from the solidus of pyrolite, *Science*, **343**, 522–525.
- Panning, M. & Romanowicz, B., 2006. A three-dimensional radially anisotropic model of shear velocity in the whole mantle, *Geophys. J. Int.*, **167**, 361–379.
- Pratt, R.G., Shin, C. & Hick, G.J., 1998. Gauss–Newton and full Newton methods in frequency–space seismic waveform inversion, *Geophys. J. Int.*, **133**, 341–362.
- Ritsema, J., Deuss, A., van Heijst, H.J. & Woodhouse, J.H., 2011. S40RTS: a degree-40 shear-velocity model for the mantle from new Rayleigh wave dispersion, teleseismic traveltime and normal-mode splitting function measurements, *Geophys. J. Int.*, **184**, 1223–1236.
- Schilling, J.-G., 1991. Flux and excess temperatures of mantle plumes inferred from their interaction with migrating mid-ocean ridges, *Nature*, **352**, 397–403.
- Simmons, N.A., Forte, A.M. & Grand, S.P., 2009. Joint seismic, geodynamic and mineral physical constraints on three-dimensional mantle heterogeneity: implications for the relative importance of thermal versus compositional heterogeneity, *Geophys. J. Int.*, **177**, 1284–1304.
- Sleep, N.H., 1990. Hotspots and mantle plumes: some phenomenology, *J. geophys. Res.*, **95**, 6715–6736.
- Stixrude, L. & Lithgow-Bertelloni, C., 2011. Thermodynamics of mantle minerals - II. Phase equilibria, *Geophys. J. Int.*, **184**, 1180–1213.
- Tackley, P.J., 2012. Dynamics and evolution of the deep mantle resulting from thermal, chemical, phase and melting effects, *Earth Sci. Rev.*, **110**, 1–25.
- Takeuchi, N., 2012. Detection of ridge-like structures in the pacific large low-shear-velocity province, *Earth planet. Sci. Lett.*, **319–320**, 55–64.
- Takeuchi, N. & Obara, K., 2010. Fine-scale topography of the d'' discontinuity and its correlation to volumetric velocity fluctuations, *Phys. Earth planet. Inter.*, **183**, 126–135.
- Takeuchi, N., Morita, Y., Xuyen, N.D. & Zung, N.Q., 2008. Extent of the low-velocity region in the lowermost mantle beneath the western Pacific detected by the Vietnamese Broadband Seismograph Array, *Geophys. Res. Lett.*, **35**, L05307, doi:10.1029/2008GL033197.
- Tarantola, A., 1987. *Inverse Problem Theory: Methods for Data Fitting and Parameter Estimation*, Elsevier.
- To, A., Romanowicz, B., Capdeville, Y. & Takeuchi, N., 2005. 3D effects of sharp boundaries at the border of the African and Pacific superplumes: observations and modeling, *Earth planet. Sci. Lett.*, **233**, 137–153.
- Trampert, J., Deschamps, F., Resovsky, J.S. & Yuen, D.A., 2004. Probabilistic tomography maps significant chemical heterogeneities in the lower mantle, *Science*, **306**, 853–856.
- Vallée, M., Charléty, J., Ferreira, A.M.G., Delouis, B. & Vergoz, J., 2011. SCARDEC: a new technique for the rapid determination of seismic moment magnitude, focal mechanism and source time functions for large earthquakes using body wave deconvolution, *Geophys. J. Int.*, **184**, 338–358.

APPENDIX A: SOURCE TIME FUNCTION

We estimate a source time function for every seismic event used in this study in order to convolve it with synthetics and

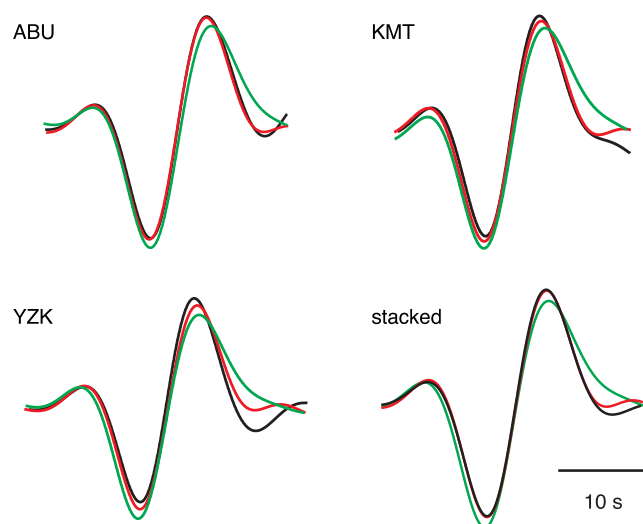


Figure A1. *S* waveforms for stations ABU, KMT, YZK and stacked waveforms of the seismic event. Black, red and green waveforms indicate observed, synthetic waveforms with the source time function computed in this study and the one by SCARDEC, respectively.

partial derivatives. The synthetic waveforms used for the estimation are computed in the same way and are filtered with a bandpass filter (0.005–0.08 Hz). We pick *S* wave peaks (up-down) in all the observed and synthetic waveforms, as shown in Fig. 2 and stack them by the centre time of the *S* peaks after normalization by the amplitude of the peaks. The observed and synthetic stacked waveforms are Fourier-transformed and source time functions are computed simply by division of them in frequency do-

main. Fig. A1 shows *S* waveforms. In order to objectively verify the estimated source time functions used in this study, we compute synthetic waveforms with a source time function by SCARDEC (Vallée *et al.* 2011). Although there are small differences, they will not affect the result in this study, because the frequency range we used samples relatively low frequencies. If extended to higher frequencies, however, a careful investigation may be required.